Analyst

ROYAL SOCIETY OF CHEMISTRY

PAPER

View Article Online
View Journal | View Issue

Cite this: *Analyst*, 2020, **145**, 5289

A new class of ratiometric small molecule intracellular pH sensors for Raman microscopy†

Liam T. Wilson, [a] William J. Tipping, [b] Lauren E. Jamieson, [b] Corinna Wetherill, [b] Zoë Henley, [c] Karen Faulds, *[b] Duncan Graham, *[b] Simon P. Mackay [d] and Nicholas C. O. Tomkinson *[a]

Intracellular pH (pH_i) homeostasis is intertwined with a myriad of normal cellular behaviors as well as pathological processes. As such, small molecule probes for the measurement of pH_i are invaluable tools for chemical biology, facilitating the study of the role of pH in cellular function and disease. The field of small molecule pH_i sensors has traditionally been dominated with probes based on fluorescent scaffolds. In this study, a series of low molecular weight (<260) oligoyne compounds have been developed which exhibit pH sensitive alkyne stretching frequencies (ν_{alkyne}) in Raman spectroscopy. The modular design of the compounds enabled tuneability of their pK_a(H) through simple structural modification, such that continuous pH sensitivity is achieved over the range 2–10. Alkyne stretching bands reside in the 'cell-silent' region of the Raman spectrum (1800–2600 cm^{-1}) and are readily detectable in a cellular environment with subcellular spatial resolution. This enabled the application of a pH sensitive oligoyne compound to the ratiometric sensing of pH_i in prostate cancer (PC3) cells in response to drug treatment. We propose that probes based on Alkyne Tag Raman Imaging offer an entirely new platform for the sensing of pH_i, complementary to fluorescence microscopy.

Received 29th April 2020,
Accepted 26th June 2020

DOI: 10.1039/d0an00865f

rsc.li/analyst

Introduction

pH homeostasis is essential for normal physiology. Regulation of both intracellular (pH_i) and extracellular (pH_e) pH plays a key role in many processes including cell proliferation[1] and differentiation,[2,3] protein synthesis,[4] the acetylation and deacetylation of histones[5] and metabolism.[6,7] Given the importance of pH in many critical functions it is unsurprising that many diseases are associated with aberrant pH profiles. For example, pH_i and pH_e dysregulation have been linked to Alzheimer's disease[8] and cancer.[9,10] The development of methods to determine the role of pH homeostasis in cellular processes and its relationship to disease is therefore of great interest.

pH_i can be determined using fluorescent probes, the most commonly used being BCECF (2′,7′-bis-(2-carboxyethyl)-5-(and-)-carboxyfluorescein)[11] and its derivatives.[12] BCECF has been used extensively in mammalian and plant cells[12–15] and living tissues,[16,17] providing accurate pH measurement and excellent sensitivity at concentrations as low as 0.1 μM.[18] However, there are limitations of BCECF and related fluorescent sensors such as photostability, phototoxicity and probe retention.[19] These deficiencies limit the use of many probes, particularly in extended real time monitoring of live cells. Whilst efforts have been made to address these problems,[12] significant challenges remain. In addition, diffuse absorption and emission spectra hinder the analysis of multiple fluorescent probes simultaneously (multiplexing), since spectral overlap limits the number of resolvable features within the spectra (especially where ratiometric sensors are used).[20,21]

Intracellular pH sensing has also been achieved by Surface Enhanced Raman Scattering (SERS) using functionalised metal nanoparticles.[22–26] These nanoparticles bear a surface coating of organic molecules with pH-dependent Raman spectra, which are detectable inside cells with excellent sensitivity, owing to the SERS effect.[27] Nanoparticle sensors, however, can suffer from reproducibility and accuracy issues arising from nanoparticle inhomogeneity,[22] and the possible

[a]*Department of Pure and Applied Chemistry, WestCHEM, Thomas Graham Building, University of Strathclyde, 295 Cathedral Street, Glasgow, G1 1XL, UK. E-mail: Nicholas.Tomkinson@strath.ac.uk*
[b]*Centre for Molecular Nanometrology, WestCHEM, Department of Pure and Applied Chemistry, Technology and Innovation Centre, University of Strathclyde, 99 George Street, Glasgow, G1 1RD, UK*
[c]*GlaxoSmithKline Medicines Research Centre, Gunnels Wood Road, Stevenage, SG1 2NY, UK*
[d]*Strathclyde Institute of Pharmacy and Biomedical Science, University of Strathclyde, 161 Cathedral Street, Glasgow, G4 0RE, UK*

†Electronic supplementary information (ESI) available: Analytical data, experimental procedures and ^{1}H, ^{19}F and ^{13}C NMR spectra for all compounds reported. Raman spectra of all compounds reported, pK_a(H) determination plots, and additional Raman data pertaining to pH measurement in PC3 cells. See DOI: 10.1039/d0an00865f

off target effects and toxicity of nanoparticles within cells remain unclear.[27] We propose that small-molecule Raman pH sensors have the potential to address these issues.

An emerging technique, which is complementary to fluorescence microscopy, is Alkyne Tag Raman Imaging (ATRI).[28,29] Alkynes have key vibrational modes that occur in the 'cell-silent' region of the Raman spectrum (1800–2600 cm^{-1}), in which few vibrational modes from endogenous biomolecules exist.[29] Alkyne bands can be detected in a cellular environment using spontaneous Raman microscopy or nonlinear variants such as Stimulated Raman Scattering (SRS).[30] The first example of ATRI in cells was the use of ethynyldeoxyuridine (EdU, **1**, Fig. 1A) which was metabolically incorporated into DNA for its visualization in cells.[28] Since then, functionalisation of small biomolecules with alkyne 'tags' has enabled visualization of the intracellular distribution of drugs,[31] natural products,[32,33] sugars[34,35] and lipids[36–38] using Raman and SRS microscopy. Alkyne-tags have also been metabolically incorporated into macromolecules such as RNA and proteins for single-step imaging by SRS.[39]

An application of ATRI that remains unexplored is the development of sensors and probes for the quantification of endogenous biomolecules and ions. A pioneering report by Min and co-workers demonstrated the suitability of chemically reactive oligoyne scaffolds in the development of a ratiometric sensor for H_2S (**2**, Fig. 1B).[20] This sensor contained an azide group in conjugation with a bisarylbutadiyne scaffold which was reduced to the corresponding aniline in the presence of H_2S. This chemical transformation induced a Raman shift change in the alkyne band, enabling the detection of intracellular H_2S by SRS microscopy. Whilst this clearly demonstrates that Raman microscopy can be used to develop intracellular sensors, it relies on an irreversible chemical process rendering the detection semi-quantitative. The development of quantitative probes for use in a cellular environment would require any change in the shift of a Raman band to be bought about through a rapid and reversible chemical transformation, such as protonation/deprotonation. Sodeoka and Fujita reported the simultaneous imaging of the protonated and deprotonated forms of carbonylcyanide *p*-trifluoromethoxyphenylhydrazone (FCCP) in HeLa cells, using a pH sensitive C≡N stretch, suggesting pH did represent a potential strategy for quantitative sensing.[40] Within this work we report bisarylbutadiynes sensitive to environmental pH, and their application to ratiometric pH_i determination by Raman microscopy (**3**, Fig. 1C). These molecules rely on reversible protonation/deprotonation events to induce a Raman shift change, enabling quantitative measurement of pH. These small molecule ratiometric pH sensors that are low molecular weight (MW <260), modular, readily tuneable, and possess good photostability,[21] represent a novel platform for pH sensing at the cellular level. Using Raman microscopy as the method for detection provides additional experimental data including a direct measure of distribution for endogenous biomolecules (proteins, lipids and nucleic acids).

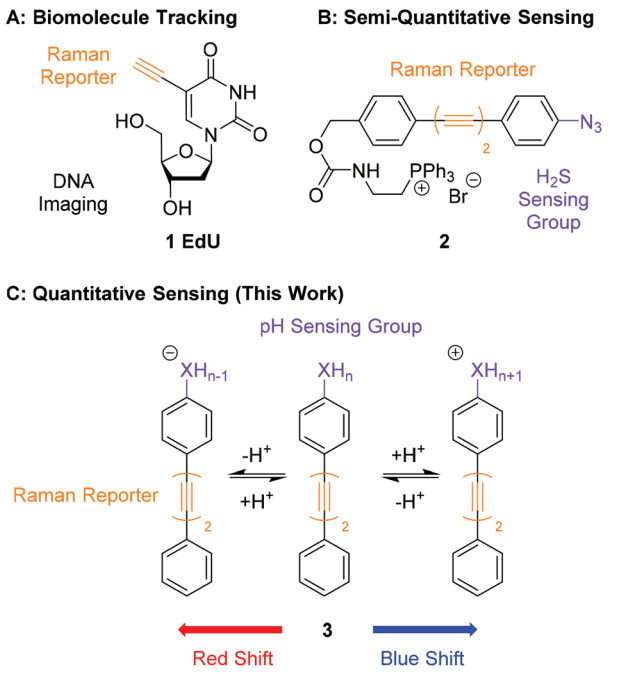

Fig. 1 Comparison of the work presented in this manuscript with previous work in ATRI. (A) Structure of EdU, first used to visualise and track intracellular DNA by Raman microscopy.[28] (B) Structure of **2**, a bisarylbutadiyne sensor of H_2S for use in SRS microscopy.[20] (C) General structure of a pH sensitive bisarylbutadiyne for quantitative pH sensing (this work).

Results and discussion

Electron delocalization influences alkyne stretching frequency

The design of our pH-sensitive probes was based around the fact that 4-ethynylaniline **4** (Fig. 2) has a lone pair of electrons on the aniline nitrogen that is in conjugation with the alkyne. Protonation of the aniline to give $\mathbf{4H^+}$ would result in the nitrogen and the alkyne no longer being conjugated. We reasoned this could manifest itself in a detectable change in the Raman

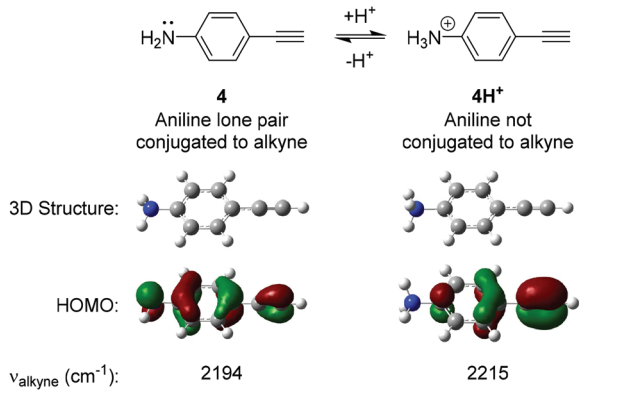

Fig. 2 Results of Density Functional Theory (DFT) calculations on 4-ethynylaniline **4** and its protonated analogue $\mathbf{4H^+}$. DFT calculations were carried out using B3LYP/6-311(G)++(d,p).

shift observed for the alkyne group. In support of this we performed DFT calculations on **4** and **4H**$^+$ which clearly showed that **4** had a significant contribution of the aniline lone pair to the calculated HOMO of the molecule whereas the aniline nitrogen made no contribution to the calculated HOMO of **4H**$^+$. Additionally, **4** displayed an unsymmetrical distribution of the HOMO across the alkyne triple bond, while distribution was more symmetrical in **4H**$^+$. The calculations suggested that the difference in the Raman stretching frequency of the two species **4** and **4H**$^+$ was $\Delta\nu_{alkyne}$ = 21 cm^{-1}. We hypothesised that the calculated sensitivity of the Raman spectrum of **4** to protonation could be exploited to develop alkyne-based probes for the determination of environmental pH.

Development of pH sensitive diynes

A bisarylbutadiyne scaffold was selected for our compounds, as it has been shown that the increased hyperpolarizability associated with the alkyne stretching vibrations of this functionality results in high Raman-scattering intensity,[21,29] giving rise to lowered detection limits in solution. We synthesised aniline **5** (Fig. 3A) and aimed to assess the sensitivity of its Raman spectrum to pH. Due to the experimental complications associated with thermodynamic pK_a(H) determination in water for hydrophobic molecules,[41] we generated pK_a(H) estimates for all compounds prepared in mixtures of 30% w/w EtOH/H_2O under conditions of constant ionic strength (I = 0.2) and temperature (20 °C). The buffer solutions used (diyne analysis buffers), and their preparation, are described in the Experimental section. The experimental pK_aH derived for **5**, and all other compounds, is valid only under the conditions of solvent, ionic strength and temperature studied. Fig. 3B shows overlays of the alkyne region of the Raman spectra of **5** at pH 1.1, 2.7 and 4.6. At pH 4.6, the unprotonated microspecies **5** dominates, and the observed ν_{alkyne} is at a minimum (2212.8 cm^{-1}) due to π-electron donation from the aniline lone pair.

Conversely, at pH 1.1, the protonated microspecies **5H**$^+$ dominates and the observed ν_{alkyne} is near maximum (2221.0 cm^{-1}) due to diminished π-electron donation. At pH 2.7, near the experimental pK_a(H), the spectrum observed is a combination of contributions from both microspecies, and the apparent ν_{alkyne} is intermediate in value (2216.4 cm^{-1}). Fig. 3C shows a plot of the apparent ν_{alkyne} of compound **5** across a range of indicated pH values. Asymptotes of the sigmoidal curve provided the maximum and minimum alkyne stretching frequency values (ν_{max} = 2221.0 and ν_{min} = 2212.8 cm^{-1}) corresponding to the peak centres of the protonated **5H**$^+$ and parent microspecies **5**, respectively. The difference between these two values is designated $\Delta\nu_{alkyne}$ (8.2 cm^{-1}). In order to determine pK_aH we assumed the observed alkyne peak at any given pH value was a linear additive combination of the peaks arising from **5** and **5H**$^+$. As shown in Fig. 3D, the combined fits effectively described the observed peaks at different pH values. The peak areas of **5** ($\mathbf{A_5}$) and **5H**$^+$ ($\mathbf{A_{5H+}}$) were determined, correcting for differing intrinsic peak intensities, allowing the mole fraction of conjugate base (χ_{Base}) to be determined as a function of pH (Fig. 5E).

Fitting the data to a Boltzmann function enabled the estimation of pK_aH from the inflection point of the sigmoid

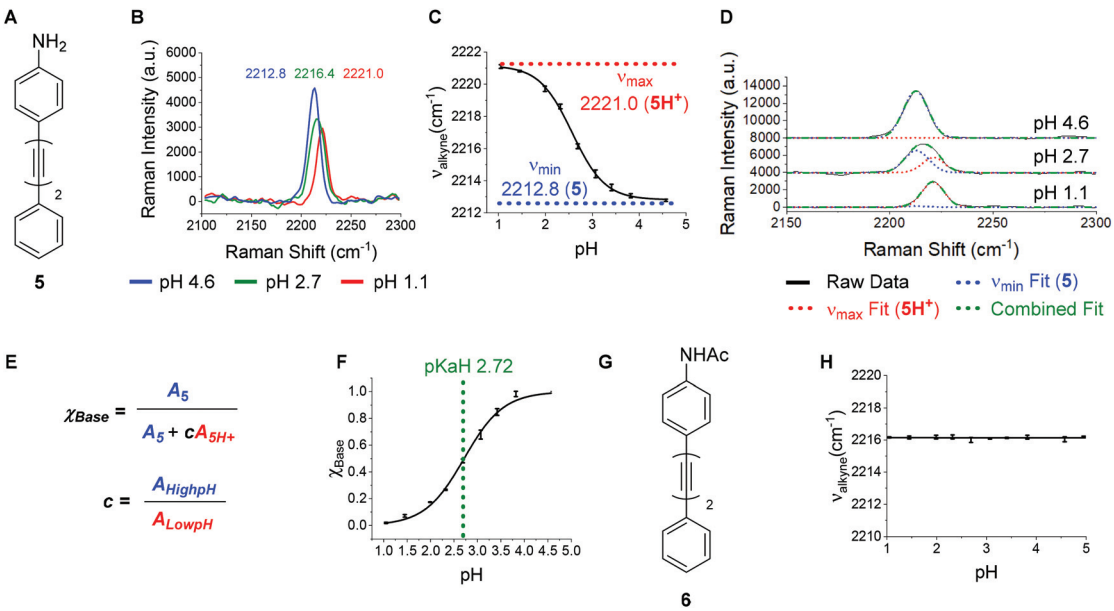

Fig. 3 (A) Structure of aniline **5**. (B) Raman alkyne peak of aniline **5** (100 μM in diyne analysis buffers, 532 nm, 1 s, 20 accumulations) at pH values 1.1 (red), 2.7 (green) and 4.6 (blue). (C) Plot of apparent ν_{alkyne} of **5** as a function of pH (n = 3, ±standard deviation) showing ν_{max} and ν_{min} values corresponding to the microspecies **5H**$^+$ and **5** respectively. Data were fitted to a Boltzmann function in OriginPro2018. (D) Curve fitting of the spectra shown in (B) using fixed peak centres associated with **5** and **5H**$^+$. Spectra are offset by 4000 a.u. in y for clarity. (E) Calculation of mole fraction of conjugate base (χ_{Base}), using peak areas derived from the curve fitting exemplified in (D). (F) Plot of χ_{Base} as a function of pH for compound **5** (n = 3, ±standard deviation). Data were fitted to a Boltzmann function in OriginPro 2018 and pK_aH is derived from the inflection point. (G) Structure of acetamide **6**. (H) Plot of apparent ν_{alkyne} of **6** (100 μM in diyne analysis buffers) as a function of pH (n = 3, ±standard deviation).

(Fig. 3F), giving a value of 2.72 ± 0.02. This pK_aH measurement of **5** was validated using UV-Visible spectroscopy under the same conditions of ionic strength and temperature (Fig. S3†), which indicated a pK_aH of 2.66, consistent within 0.06 units of the value obtained by Raman, providing strong confidence in the methods used.

To test the hypothesis that the pH sensitivity of ν_{alkyne} exhibited by **5** could be attributed to aniline protonation, we synthesised the corresponding acetamide **6** (Fig. 3G). Pleasingly, **6** showed no change of the ν_{alkyne} over the pH range 1.1–5.0 (Fig. 3H). In line with our hypothesis we attribute this to the absence of a basic nitrogen lone pair.

Encouraged by the positive results obtained with aniline **5**, we synthesised a series of diyne compounds **7–18** which exhibited pH sensitivity in different ranges (Fig. 4). Compounds were designed to incorporate aromatic substituents in conjugation with the diyne moiety which could be expected to influence π-electron density within the molecule. In addition, substituents were selected which had an expected pK_a(H) 2–10, with the rationale that protonation/deprotonation events in solution would influence π-electron density in the alkyne chain, and in turn the observed ν_{alkyne}. Plots of ν_{alkyne} variance as a function of pH were constructed for compounds **7–18** (Fig. S4†). As predicted, compounds **5** and **7–18** showed sigmoidal relationships between ν_{alkyne} and environmental pH, and pK_a(H) values could be determined using the multiple curve fitting method discussed previously. Plots of χ_{Base} as a function of pH can be found in Fig. S5.† Fig. 4 details the apparent pK_a(H), ν_{max}, ν_{min} and $\Delta\nu_{alkyne}$ values for compounds **5** and **7–18**. As discussed above, aniline **5** showed a pK_aH of 2.7 and a decrease in ν_{alkyne} with increasing pH, consistent with an increasing proportion of the microspecies **5** (decreasing $\mathbf{5H^+}$). Aniline **7** showed a similar trend. Notably, **7** exhibited an increased pK_aH (3.2) and diminished $\Delta\nu_{alkyne}$ (4.6, compared to 8.2 for **5**), likely arising from reduced conjugation due to the *meta*-substitution pattern.

Unlike most compounds studied, pyridine derivative **8** (pK_aH = 3.3) showed an increase of ν_{alkyne} with increasing pH.

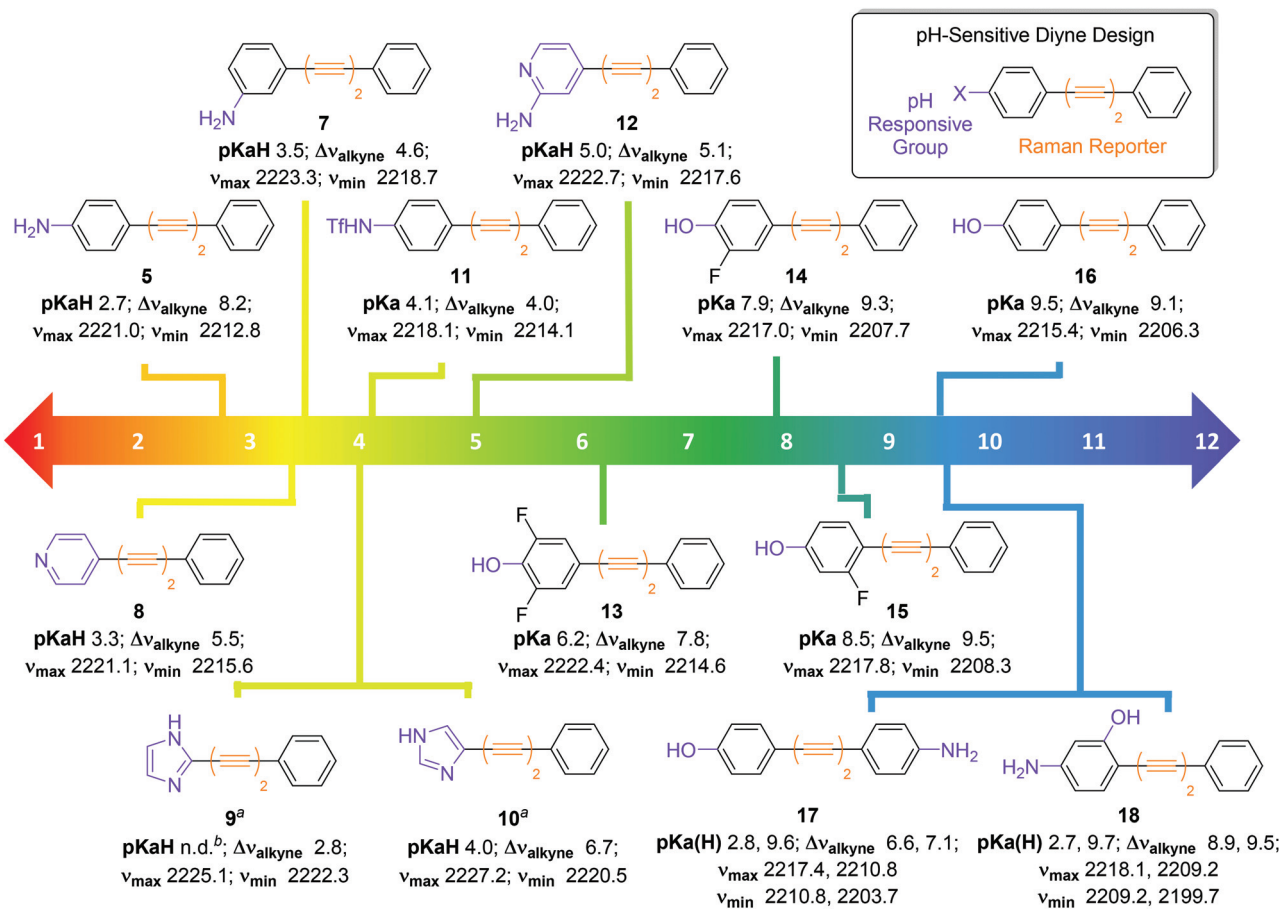

Fig. 4 Design and structures of diyne compounds **5** and **7–18** showing experimental pK_a(H), ν_{max}, ν_{min} and $\Delta\nu_{alkyne}$ values. Data were derived from plotting mean ν_{alkyne} values (n = 3, ±standard deviation) of **5** and **7–18** (100 μM in diyne analysis buffers) as a function of pH. Curves were fitted to Boltzmann functions in OriginPro 2018 and asymptotes afforded ν_{max}, ν_{min} and $\Delta\nu_{alkyne}$ values. Multiple peak fitting in OriginPro2018 at fixed peak centres derived from ν_{max} and ν_{min} enabled determination of A_{Base} and A_{Acid} as a function of pH, and values of A_{HighpH} and A_{LowpH} were derived from spectra at extreme pH values. Plots of χ_{Base} as a function of pH were constructed according to eqn (1), and data were fitted to Boltzmann functions. pK_a(H) values were derived from the inflection points of these curves. Notes: [a]Experiments carried out at a compound concentration of 200 μM; [b]pK_aH could not be determined.

We reason that, given the π-deficient electron withdrawing nature of the pyridine ring, protonation of the nitrogen atom induced increased conjugation with the alkynes, which resulted in a decreased stretching frequency for the microspecies **8H**$^+$. Imidazoles **9** and **10** showed the opposite trend to the pyridine species **8**, as the protonated microspecies **9H**$^+$ and **10H**$^+$ exhibited increased ν_{alkyne} upon protonation. We reason that, as imidazoles are π-excessive and electron donating, protonation induced decreased conjugation with the alkyne. We were unable to accurately determine a pK_aH value for imidazole **9** as multiple curve fitting reported inconsistent values for A_{Base} and A_{Acid}, likely due to the small $\Delta\nu_{alkyne}$ of 2.8.

Triflamide **11** (pK_a = 4.1) displayed a decrease in ν_{alkyne} on increasing pH, as the deprotonated analogue of **11** is expected to have increased conjugation with the alkyne chain. Aminopyridine **12** exhibited a pH dependence in line with that of pyridine **8**, displaying a predictably higher pK_aH (5.0). Phenols **13–16** exhibited a decrease in ν_{alkyne} upon increasing pH consistent with an increased π-electron delocalization upon deprotonation to the phenolate. It is noteworthy that the observed pK_a values of these compounds were readily tuneable by incorporation of inductively withdrawing fluorine atoms in proximity to the phenolic oxygen allowing variance in the observed pK_a of >3 pH units (*cf.* compounds **13** and **16**).

It also proved possible to include two pH sensitive groups within the molecule providing two pK_a(H) values for a single compound. For example, the bifunctional molecule **17**, which contains an aniline and a phenol group on different aromatic rings displayed two discrete inflection points, the first at the pK_aH of the aniline (2.8) and the second at the pK_a of the phenol (9.6). The related compound **18**, where the two functional groups are on the same aromatic ring, also showed inflection points for the aniline (pK_aH = 2.7) and the phenol (pK_a = 9.7). With the ability to finely tune pK_a(H) values by the introduction of either electron donating or electron withdrawing groups on the aromatic ring(s), bespoke pH probes can be designed to provide sensitivity over multiple pH ranges.

The modular design of compounds **5** and **7–18** enabled rational tuning of their pK_a(H) by substitution of the pH responsive group. Between the 14 diyne compounds prepared, there are compounds capable of pH-sensitivity for any pH value between 2–10 and this work provides the foundation for the design of oligoyne pH sensors for Raman microscopy across the physiological pH range. We have shown that detectable changes in ν_{alkyne} (3–18 cm^{-1}) can be induced by protonation/deprotonation events. Other researchers have shown[22,24,37] that larger changes in the base ν_{alkyne} values of oligoynes can be engineered by isotopic labelling of alkynes (>20 cm^{-1}), and increasing the number of alkyne groups present in the molecule (>40 cm^{-1}). It stands to reason, therefore, that the use of pH sensitive oligoynes with different alkyne chain lengths could enable visualization of multiple species simultaneously, with complete resolution, to enable multiplexing of multiple pH sensors, designed to report on discrete microenvironments.

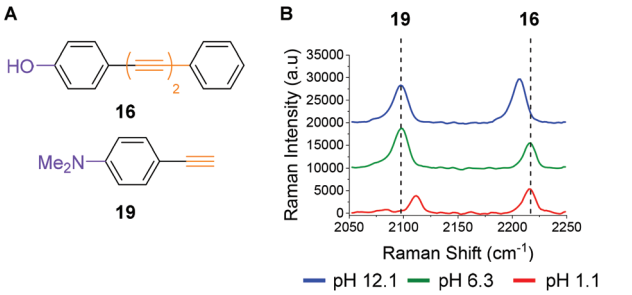

Fig. 5 (A) Structures of phenol **16** and dimethylaniline **19**. (B) Raman spectra of phenol **16** (100 μM in diyne analysis buffers, 532 nm, 1 s, 20 accumulations) and dimethylanline **19** (5 mM in diyne analysis buffers) at pH values 1.1, 6.3 and 12.1. Spectra have been cropped to show the alkyne region and offset by 10 000 a.u. in the *y* axis for clarity.

To illustrate the potential for multiplexing, we captured spectra of phenol **16** and commercially available dimethylaniline derivative **19** (Fig. 5A) in a single solution at different pH values (Fig. 5B). The Raman peaks corresponding to the alkyne group(s) of both compounds are clearly resolved at pH 12.1 (blue line), pH 6.3 (green line) and pH 1.1 (red line), enabling visualization of pH sensitivity for both compounds. The spectra indicate that at high pH (12.1) a different microspecies of compound **16** is present in solution when compared to the spectra obtained at lower pH (6.3 and 1.1). They also indicate that at low pH (1.1) dimethylaniline derivative **19** is present as a different microspecies to the spectra recorded at higher pH (6.3 and 12.1). These experiments show that through judicious design multiplexing of pH sensitive Raman probes should be possible.

Intracellular pH sensing

For the purposes of developing an intracellular pH sensor, compounds with pK_a(H) values close to physiological pH ranges were desirable.[6] The apparent pK_a(H) values reported in Fig. 4 served as a guide for assessing suitability of the diyne compounds for intracellular pH sensing. Based on the data accrued, phenol **13** appeared to be a promising candidate for use as a cytosolic pH sensor due to its apparent pK_a of 6.2 (Fig. 6A). Prior to investigation within a cellular environment, the photostability of **13** in solution was established by acquiring 120 consecutive spectra (acquisition time = 0.5 s) followed by integration of the alkyne peak using OriginPro 2018 (Fig. S6†). In addition, **13** was evaluated for any potential cellular toxic effect. Exposure of PC3 cells to 25 μm **13** for 6 h showed no change in cell count when compared to a DMSO control (Fig. S7†).

To quantitatively determine pH, **13** required calibration within the environment of interest. For the purposes of cellular pH sensing, the method of Thomas[42] was used to calibrate our selected compound. Nigericin is an H^+/K^+ ion transporter which is commonly used to calibrate fluorescent pH probes.[18,43,44] Cells were treated with **13** (25 μM, 30 min), and nigericin (25 μM) was used to equilibrate pH_i with pH_e in high

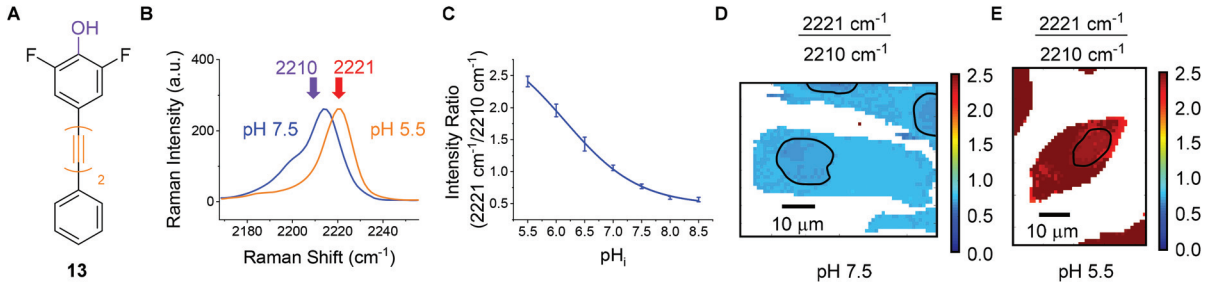

Fig. 6 Raman imaging of PC3 cells treated with phenol **13** (25 μM, 30 min) fixed to discrete pH_i values using the method of Thomas.[42] (A) Structure of phenol **13**. (B) Overlaid sample spectra from PC3 cells fixed to pH_i 7.5 (blue) and 5.5 (orange). Spectra are presented within the range 2170–2260 cm^{-1} and normalised to the maximum intensity within that range. (C) Calibration curve for **13** in PC3 cells. Average 2221/2210 cm^{-1} intensity ratios from PC3 cells (n = 5, ±standard deviation, 532 nm, 0.5 s, 5 μm step size in x and y) were plotted at the indicated pH_i values. Data were fitted to a Boltzmann function in OriginPro 2018. (D) and (E) False colour images representing the 2221/2210 cm^{-1} signal intensity ratios (532 nm, 0.5 s, 1 μm step size in x and y), in PC3 cells, fixed to pH_i 7.5 and 5.5 respectively. The nuclear regions are highlighted by black bands.

K^+ buffer solutions at pH values of 5.5, 6.0, 6.5, 7.0, 7.5, 8.0 and 8.5. The cells were then imaged using a Raman microscope. Under these conditions ν_{max} and ν_{min} were determined to be 2221 cm^{-1} and 2210 cm^{-1} respectively. Fig. 6B shows sample spectra from PC3 cells treated with **13** (25 μM, 30 min) and fixed to the pH_i values of 5.5 (orange) and 7.5 (blue), illustrating the change in spectroscopic properties of **13** in response to pH_i. Fig. 6C shows a plot of average 2221/2210 cm^{-1} signal intensity ratios derived from Raman maps of PC3 cells across the pH_i range measured (n = 5 cells per condition, 5 μm step size in x and y, ±standard deviation). The data were fitted to a Boltzmann function to generate a calibration curve, enabling us to relate the 2221/2210 cm^{-1} ratio of **13** to pH_i. Fig. 6D and E show false colour images of the 2221/2210 cm^{-1} ratio in PC3 cells fixed to pH 7.5 and 5.5 respectively. The Raman maps from which these derive were acquired at a resolution of 1 μm in x and y. These false colour images, and all others reported in this manuscript and ESI† were generated using a custom MATLAB® script reported in previous publications.[38,45] As with fluorescent sensors, a minimum intensity cut-off should be established prior to ratiometric analysis, because ratios vary significantly as signal intensity decreases toward the threshold of detection.[19] We established that the signal intensity of **13** was lowest within cell nuclei (Fig. S9†), due to minimal nuclear penetration of the probe compounds. This distribution pattern is consistent with analogous oligoyne molecules.[21,29,32,33] As such, although the 2221/2210 cm^{-1} ratio appears to be consistent throughout the cells in Fig. 6D and E, we chose to exclude nuclear regions from interpretation and these are highlighted by black bands.

It is clear, however, from Fig. 6D and E that the 2221/2210 cm^{-1} ratio is consistent throughout the cytoplasm of the PC3 cells and varies as a function of pH_i. Having calibrated **13** within a cellular environment, we aimed to determine whether this probe could be used to monitor and quantify changes in pH_i in response to drug treatment. It has been reported that apoptosis is accompanied by a decrease in pH_i.[46] Treatment of 6 plates of PC3 cells with etoposide (80 μg mL^{-1}, 30 min) induced apoptosis.[47] Following incubation periods of 0.5, 1.5, 2.5, 3.5, 4.5 or 5.5 h, **13** (25 μM) was added and the cells were imaged after a further 30 minutes (n = 6 cells per time point, 532 nm, 0.5 s, 5 μm step size in x and y). From these data the 2221/2210 cm^{-1} ratio was extracted from average spectra at each time point and related to pH_i using the calibration curve shown in Fig. 6C. Fig. 7A shows a plot of pH_i over time. The average 2221/2210 cm^{-1} ratio at 0 h (no etoposide treatment) of 0.843 ± 0.027, corresponds to a pH_i of 7.34 ± 0.05. The pH_i steadily decreased over time, reaching a minimum at 4 h of 7.13 ± 0.08 (***p < 0.01), before showing signs of recovery. The change in pH and cellular recovery is consistent with observations with HL-60 cells.[47,48] This experiment was repeated, with consistent results (Fig. S10†). For visual clarification, high resolution maps (1 μm step size in x and y) were acquired at the 0 and 4 h time points. Fig. 7B and C show false colour representations of the 2221/2210 cm^{-1} ratio in PC3 cells at 0 h and 4 h respectively. As before (*cf.* Fig. 6), low alkyne signal was observed in the nuclear regions of these cells (Fig. S11†), and so pH_i data in these regions (highlighted by black bands) was excluded from interpretation. It is clear that the cell at 4 h post etoposide treatment (Fig. 7C) has a higher 2221/2210 cm^{-1} ratio and thus lower pH_i than the cell at 0 h (Fig. 7B), in agreement with the data in Fig. 7A, showing that **13** can be used to effectively monitor and quantify changes in pH_i of live cells in response to drug treatment.

A distinct advantage of Raman spectroscopy over other cellular imaging techniques is the rich information provided on compartmentalisation, the location of organelles and the distribution of endogenous biomolecules such as lipids and proteins. This is determined in a label free manner, therefore, each piece of experimental data gathered within this investigation provides considerable further knowledge, as demonstrated by identification of nuclear regions through lipid to protein ratio analysis (Fig. S9 and S11†) This data could not be obtained using spontaneous Raman microscopy in conjunc-

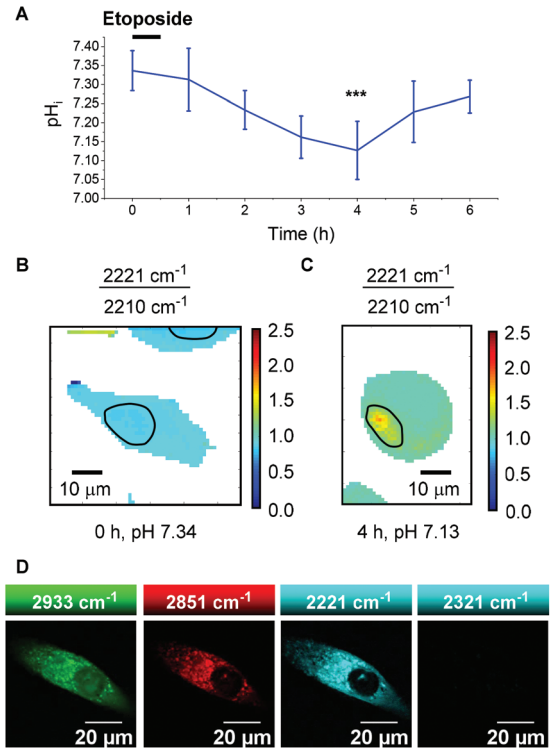

Fig. 7 Measurement of pH_i changes over time in PC3 cells treated with etoposide. 6 cell plates were treated with etoposide (80 µg mL^{-1}, 30 min) and incubated for varying times of 0.5, 1.5, 2.5, 3.5, 4.5 or 5.5 h, prior to analysis. Cells were treated with **13** (25 µM, 30 min) before analysis. (A) Plot of average PC3 cell pH_i as a function of time (n = 6 cells, ±standard deviation). The 0 h time point represents no etoposide treatment. Values derive from the average 2221/2210 cm^{-1} ratio (n = 6 cells, 532 nm, 0.5 s, 5 µm step size in x and y, ±standard deviation) (***p < 0.01, Student's t test). (B) False color image representing the 2221/2210 cm^{-1} ratio in a single PC3 cell at time 0 h (532 nm, 0.5 s, 1 µm step size in x and y). Nuclear regions are highlighted by black bands. (C) False color image representing the 2221/2210 cm^{-1} ratio in a single PC3 cell at time 4 h (1 µm step size in x and y). The nuclear region is highlighted by a black band. (D) Imaging of **13** (25 µM, 30 min) in live PC3 cells by SRS microscopy. Images were acquired in sequence 2933 cm^{-1} (CH_3, proteins), 2851 cm^{-1} (CH_2, lipids), 2221 cm^{-1} (alkyne, **13**), 2321 cm^{-1} (off-resonance). Images acquired at 512 × 512 pixels, 10 µs pixel dwell time with false colours applied to different detection wavenumbers.

tion with a fluorescent probe, due to photobleaching, and the obscuring of Raman data by the fluorescence response.

To demonstrate the compatibility of **13** with advanced Raman imaging techniques, live PC3 cells were treated with **13** (25 µM, 30 min) and imaged by SRS microscopy for improved spatial resolution. Fig. 7D shows false colour images of 2933 cm^{-1} (CH_3, protein), 2951 cm^{-1} (CH_2, lipid), 2221 cm^{-1} (alkyne, **13**) and 2321 cm^{-1} (off-resonance) channels in a single PC3 cell. The 2221 cm^{-1} channel confirms the extranuclear, cytoplasmic distribution of **13** with subcellular resolution, demonstrating the compatibility of this probe of this probe for intracellular pH sensing. We aim to extend the current capability of this probe by performing ratiometric SRS imaging for high-resolution pH sensing.

Experimental

DFT calculations

DFT calculations were performed using the Gaussian09 suite of programs.[49] Structures were optimised and then characterised using frequency calculations at the B3LYP/6-311(G)++(d,p) level of theory.

Buffer preparation

Diyne analysis buffers. A series of Britton–Robinson buffers were prepared in 30 wt%. EtOH to a constant ionic strength (I) of 0.2 by addition of KCl, according to the method of Mongay and Cedra.[50] The pH values of the prepared solutions were measured using a Jenway Model 2510 pH meter, and adjusted for the solvent effect according to correction values reported by Gelsema *et al.*[51] Final, corrected pH values for buffer solutions were: 1.99, 2.32, 2.69, 3.07, 3.41, 3.82, 4.57, 4.95, 5.34, 5.77, 6.27, 6.85, 7.51, 8.17, 8.74, 9.35, 9.94, 10.45, 10.90, 11.50 and 12.05. In order to access the pH range 1–2, HCl/KCl buffers were prepared from 3 : 1 and 1 : 1 mixtures of 0.2 M HCl and 0.2 M KCl in 30 wt%. EtOH, to give corrected[51] pH values of 1.05 and 1.45 respectively.

High K^+ buffers for nigericin calibration. Aqueous buffers containing 135 mM KCl, 2 mM K_2HPO_4, 20 mM HEPES, 1.2 mM $CaCl_2$ and 0.8 mM $MgSO_4$ were prepared, and adjusted to the pH values of 5.50, 6.00, 6.50, 7.00, 7.50, 8.00 and 8.50 by the addition of 1 M HCl or NaOH.

Cell culture. PC3 cells (human prostate adenocarcinoma) were gifted from the Strathclyde Institute of Pharmacy and Biomedical Sciences (Glasgow) as a subculture from a stock received from the European Collection of Authenticated Cell Cultures (ECACC).

pH sensor calibration. PC3 cells were plated on 35 mm glass-bottomed culture dishes (Ibidi) in DMEM at a concentration of 5 × 10^5 cells per mL and incubated at 37 °C and 5% CO_2 for 24 h prior to treatment. Cells were treated with 25 µM **13** from a 10 mM stock solution in DMSO and incubated for 30 min at 37 °C and 5% CO_2. Dishes were then aspirated and washed twice with high K^+ buffer solution at the required pH. High K^+ buffer solution containing 25 µM nigericin at the required pH was then added to the plates, which were incubated at 37 °C and 5% CO_2 for 5 min prior to imaging.

pH measurement. PC3 cells were plated on 35 mm glass-bottomed culture dishes (Ibidi) in DMEM at a concentration of 5 × 10^5 cells per mL and incubated at 37 °C and 5% CO_2 for 24 h prior to treatment. Cells were treated with 25 µM **13** from a 10 mM stock solution in DMSO and incubated for 30 min at 37 °C and 5% CO_2. Dishes were then aspirated and washed twice with PBS, before refilling with PBS prior to imaging.

For etoposide treatment experiments, cells in 6 separate dishes were treated with 80 µg mL^{-1} etoposide from a 16 mg mL^{-1} stock solution in DMSO for and incubated for 30 min at 37 °C and 5% CO_2. Dishes were aspirated and washed twice with PBS and refilled with DMEM. Each dish was incubated for a further time of 0.5, 1.5, 2.5, 3.5, 4.5 or 5.5 h at 37 °C and 5% CO_2. Incubation periods were interrupted 30 min prior to

their end point and cells were treated with 25 μM **13**, then returned to the incubator for 30 min. Then they were then aspirated and washed twice with PBS, before refilling with PBS prior to imaging.

SRS microscopy. PC3 cells were plated on high precision glass coverslips (#1.5H Thickness, 22 × 22 mm, Thorlabs) in a 6-well plate in DMEM at a concentration of 5×10^5 cells per mL and incubated at 37 °C and 5% CO_2 for 24 h prior to treatment. Cells were treated with 25 μM **13** from a 10 mM stock solution in DMSO and incubated for 30 min at 37 °C and 5% CO_2. Plates were then aspirated and washed twice with PBS. Coverslips were then affixed to glass microscope slides with a PBS boundary between the glass layers prior to imaging.

Raman spectroscopy

All Raman spectra were acquired on a Renishaw inVia Raman microscope equipped with a 532 nm Nd:YAG laser giving a maximum power of 500 mW, 1800 lines per mm grating. Prior to spectral acquisitions, the instrument was calibrated using the internal silicon standard at 520 cm^{-1}.

Neat compounds. A small amount of sample compounds **5–19** were transferred onto a CaF_2 window and spectra were acquired using an Olympus 20×/NA 0.40 NPlanEPI objective, an acquisition time of 1 s, a laser power of 1% (*ca.* 0.2 mW) and 10 accumulations with a spectral centre of 1600 cm^{-1}. 3 measurements were taken for each sample.

Experimental pK_a(H) determinations. Wells of a 96 well plate were charged with a stock solution of alkyne compound **5–19** (0.7 μL, 50 mM, EtOH) and diluted to 350 μL using diyne analysis buffers at the desired pH values. The resulting final concentrations of **5–19** were 100 μM (unless otherwise stated). Samples were equilibrated to a room temperature of 20 °C prior to spectral acquisition. Spectra were acquired of each solution using a 20×/NA 0.40 NPlanEPI objective, a laser power of 100% (*ca.* 20 mW), acquisition time of 1 s, with 20 accumulations and a spectral centre of 1800 cm^{-1}. 3 measurements were taken per condition.

pH sensor calibration cell maps. PC3 cells in glass bottomed culture dishes (Ibidi), prepared as described previously were mapped using a Nikon 60×/NA 1.0 NIR Apo water immersion objective, with a 5 μm step size in x and y, 0.5 s acquisition time, 100% laser power (*ca.* 17 mW) and a spectral centre of 2500 cm^{-1}. 5 maps of different cells were acquired from a single culture plate for each condition. Note: to ensure reproducibility, the spectrometer was calibrated regularly (every 30 min) using the internal silicon standard during these experiments.

pH measurement cell maps. PC3 cells in glass bottomed culture dishes (Ibidi), prepared as described previously were mapped using a Nikon NIR Apo 60× water immersion objective, with a 5 μm step size in x and y, 0.5 s acquisition time, 100% laser power (*ca.* 17 mW) and a spectral centre of 2500 cm^{-1}. 6 maps of different cells were acquired from a single culture dish per condition. For the high-resolution images presented in the Fig. 6 and 7, additional maps were generated using a 1 μm step size in x and y. Note: to ensure reproducibility, the spectrometer was calibrated regularly (every 30 min) using the internal silicon standard during these experiments.

Stimulated Raman scattering microscopy

An integrated laser system (picoEMERALD™ S, Applied Physics & Electronics, Inc.) was used to produce two synchronised laser beams at 80 MHz repetition rate. A fundamental Stokes beam (1031.4 nm, 2 ps pulse width) was intensity modulated by an electro-optic-modulator with >90% modulation depth, and a tunable pump beam (700–960 nm, 2 ps pulse width, <1 nm (10 cm^{-1}) spectral bandwidth) was produced by a built-in optical parametric oscillator. The pump and Stokes beams were spatially and temporally overlapped using two dichroic mirrors and a delay stage inside the laser system and coupled into an inverted laser-scanning microscope (Leica TCS SP8, Leica Microsystems) with optimised near-IR throughput. SRS images were acquired using 40× objective (HC PL IRAPO 40×, N.A. 1.10 water immersion lens) with a 10 μs pixel dwell time over a 512 × 512 frame. The Stokes beam was modulated with a 20 MHz EoM (Zurich Instruments). Forward scattered light was collected by a S1 N. A. 1.4 condenser lens (Leica Microsystems). Images were acquired at 8-bit image depth. The laser powers measured after the objective lens were in the range 10–30 mW for the pump beam only, 10–50 mW for the Stokes beam only and 20–70 mW (pump and Stokes beams).

UV-Visible spectroscopy

Solutions of **5** and **11** were prepared using by diluting an aliquot from a stock solution (2 μL, 12.5 mM, EtOH) to a volume of 1 mL using diyne analysis buffer at the desired pH. The resulting final concentration of **5** or **11** was 25 μM. Samples were equilibrated to a room temperature of 20 °C prior to spectral acquisition. Spectra were recorded using an Agilent Cary 60 UV-Visible spectrometer between 250 and 800 nm at a resolution of 0.5 nm.

Data processing

Single spectra. All spectra were processed using WiRE 4.4™. Spectral baselines were subtracted, and smoothing was achieved using Savitzky–Golay filtering with a polynomial order of 3 and a frame length of 9. Peak centres and intensity values were ascertained using the Lorentzian function built into the curve-fit tool.

Experimental pK_a(H) determinations by Raman spectroscopy. Alkyne stretching frequency values of **5** and **7–18** as a function of pH were plotted in OriginPro2018 and fitted to a Boltzmann function. From the output, ν_{max} and ν_{min} values were determined from asymptotes. Spectra of **5**, and **7–18** at different pH values were subjected to curve fitting analysis using the peak analysis tool in OriginPro 2018. For each spectrum, analysis was performed on the 2100–2300 cm^{-1} region, and spectral baselines were established by interpolation over 20 points. 2 peaks were fitted using Gaussian functions, at fixed peak centres defined by the ν_{max} and ν_{min} values of the

compound. Bounds were set such that the area of each peak must be ≥0, and all other curve parameters were left variable. The resulting peak areas arising from the conjugate acid (A_{Acid}) and base (A_{Base}) microspecies were recorded for each spectrum. The parameters A_{HighpH} and A_{LowpH} were derived from average total peak areas (n = 3) at extreme pH values for each compound. Average χ_{Base} values (n = 3) were then plotted as a function of pH for each compound according to eqn (1), where c is A_{HighpH}/A_{LowpH}.

$$\chi_{Base} = \frac{A_{Base}}{A_{Base} + c(A_{Acid})} \quad (1)$$

These data were fitted to Boltzmann functions in OriginPro 2018, and pK_a(H) values were derived from inflection points.

Experimental pK_a(H) determinations by UV-Visible spectroscopy. Data were exported as an Excel file and transferred to OriginPro 2018, within which intensity values were extracted, and the 340/306 nm ratio (**5**) or 340/293 nm ratio (**11**) were recorded. Data were then plotted according to eqn (2).[48]

$$pH = pK_a + c\left[\log\frac{R - R_{min}}{R_{max} - R}\right] + \log\frac{I_a}{I_b} \quad (2)$$

R is the ratio of emission intensity at two wavelengths. R_{max} and R_{min} are maximum and minimum limiting values of R (determined from the asymptotes of plots of R *vs.* pH), and c is the slope. I_a/I_b is the ratio of the absorption intensity in acid to the absorption intensity in base at the wavelength chosen for the denominator of R.[52] pK_a(H) was determined from the y intercept minus log(I_a/I_b).

Cell maps. Cosmic rays were removed using a nearest neighbour algorithm and noise filtering was carried out prior to other processing. To determine average pH_i values in cells, average spectra were computed from map data, from which intensities at 2210 and 2221 cm^{-1} were extracted. The intensity ratio maps shown in Fig. 6, 7, S6 and S7† were generated using a custom MATLAB® script reported in previous publications.[38,45]

SRS images. Images were assigned false colours using ImageJ, and scale bars were applied. Brightness settings were unadjusted for the 2933 cm^{-1} and 2851 cm^{-1} images, while the 2221 cm^{-1} and 2321 cm^{-1} images were scaled between 0 and 125 units.

Conclusions

In summary, we have reported the development of a bespoke suite of low molecular weight diyne compounds which exhibit pH sensitive Raman spectra. Using a modular design strategy, the pK_a(H) values of the series were tuned to achieve sensitivity across a physiologically-relevant pH range (2–10) in order to detect and monitor changes in pH. Following calibration, we demonstrated that compound **13** could be used to ratiometrically determine pH_i in PC3 cells and, significantly, to monitor change in pH_i in response to a homeostatic disruptor, in this case exemplified by administration of the chemotherapeutic agent etoposide. The probe molecule **13** proved to be photostable, non-toxic and cell penetrant, providing the first example of an environmentally sensitive small molecule to enable accurate pH determination by Raman microscopy. Central to the success of these quantitative probes was the use of a rapid and reversible chemical equilibrium to influence the Raman spectrum of the bioorthogonal alkyne. The ability to use Raman microscopy for quantitative sensing using ratiometric probes represents an exciting new application of ATRI which could be used to detect other important ions and biomolecules of relevance to disease. We believe that the work presented here represents an entirely novel platform for pH sensing in a cellular environment which will find broad applicability in the chemical and life sciences.

Conflicts of interest

There are no conflicts to declare.

Acknowledgements

We thank the University of Strathclyde, the EPSRC and GlaxoSmithKline for financial support. We are extremely grateful to Dr Alison Nordon for her insight and advice in curve fitting analysis to determine experimental pK_a(H) values.

Notes and references

1 M. Flinck, S. H. Kramer and S. F. Pedersen, *Acta Physiol.*, 2018, **223**, e13068.
2 J. D. Gross, J. Bradbury, R. R. Kay and M. J. Peacey, *Nature*, 1983, **303**, 244–245.
3 B. Ulmschneider, B. K. Grillo-Hill, M. Benitez, D. R. Azimova, D. L. Barber and T. G. Nystul, *J. Cell Biol.*, 2016, **215**, 345–355.
4 S. J. Fuller, C. J. Gaitanaki and P. H. Sugden, *Biochem. J.*, 1989, **259**, 173–179.
5 M. A. McBrian, I. S. Behbahan, R. Ferrari, T. Su, T.-W. Huang, K. Li, C. S. Hong, H. R. Christofk, M. Vogelauer, D. B. Seligson and S. K. Kurdistani, *Mol. Cell*, 2013, **49**, 310–321.
6 J. R. Casey, S. Grinstein and J. Orlowski, *Nat. Rev. Mol. Cell Biol.*, 2010, **11**, 50–61.
7 W. B. Busa and R. Nuccitelli, *Am. J. Physiol.: Regul., Integr. Comp. Physiol.*, 1984, **246**, R409–R438.
8 T. A. Davies, R. E. Fine, R. J. Johnson, C. A. Levesque, W. H. Rathbun, K. F. Seetoo, S. J. Smith, G. Strohmeier, L. Volicer, L. Delva and E. R. Simons, *Biochem. Biophys. Res. Commun.*, 1993, **194**, 537–543.
9 M. Schindler, S. Grabski, E. Hoff and S. M. Simon, *Biochemistry*, 1996, **35**, 2811–2817.
10 H. Izumi, T. Torigoe, H. Ishiguchi, H. Uramoto, Y. Yoshida, M. Tanabe, T. Ise, T. Murakami, T. Yoshida, M. Nomoto and K. Kohno, *Cancer Treat. Rev.*, 2003, **29**, 541–549.

11 T. J. Rink, *J. Cell Biol.*, 1982, **95**, 189–196.
12 J. Han and K. Burgess, *Chem. Rev.*, 2010, **110**, 2709–2728.
13 T. Speake and A. C. Elliott, *J. Physiol.*, 1998, **506**, 415–430.
14 A. Varadi and G. A. Rutter, *Endocrinology*, 2004, **145**, 4540–4549.
15 D. Pérez-Sala, D. Collado-Escobar and F. Mollinedo, *J. Biol. Chem.*, 1995, **270**, 6235–6242.
16 I. D. Weiner and L. L. Hamm, *Am. J. Physiol.: Renal, Fluid Electrolyte Physiol.*, 1989, **256**, F957–F964.
17 C. Hille, M. Berg, L. Bressel, D. Munzke, P. Primus, H.-G. Löhmannsröben and C. Dosche, *Anal. Bioanal. Chem.*, 2008, **391**, 1871–1879.
18 P. A. Valant and D. H. Haynes, *J. Fluoresc.*, 1992, **2**, 191–206.
19 B. K. Grillo-Hill, B. A. Webb and D. L. Barber, in *Methods in Cell Biology*, Elsevier, 2014, vol. 123, pp. 429–448.
20 C. Zeng, F. Hu, R. Long and W. Min, *Analyst*, 2018, **143**, 4844–4848.
21 F. Hu, C. Zeng, R. Long, Y. Miao, L. Wei, Q. Xu and W. Min, *Nat. Methods*, 2018, **15**, 194–200.
22 C. E. Talley, L. Jusinski, C. W. Hollars, S. M. Lane and T. Huser, *Anal. Chem.*, 2004, **76**, 7064–7068.
23 J. Kneipp, H. Kneipp, B. Wittig and K. Kneipp, *J. Phys. Chem. C*, 2010, **114**, 7421–7426.
24 J. Kneipp, H. Kneipp, B. Wittig and K. Kneipp, *Nano Lett.*, 2007, **7**, 2819–2823.
25 A. Pallaoro, G. B. Braun, N. O. Reich and M. Moskovits, *Small*, 2010, **6**, 618–622.
26 L. E. Jamieson, A. Jaworska, J. Jiang, M. Baranska, D. J. Harrison and C. J. Campbell, *Analyst*, 2015, **140**, 2330–2335.
27 C. Zong, M. Xu, L.-J. Xu, T. Wei, X. Ma, X.-S. Zheng, R. Hu and B. Ren, *Chem. Rev.*, 2018, **118**, 4946–4980.
28 H. Yamakoshi, K. Dodo, M. Okada, J. Ando, A. Palonpon, K. Fujita, S. Kawata and M. Sodeoka, *J. Am. Chem. Soc.*, 2011, **133**, 6102–6105.
29 H. Yamakoshi, K. Dodo, A. Palonpon, J. Ando, K. Fujita, S. Kawata and M. Sodeoka, *J. Am. Chem. Soc.*, 2012, **134**, 20681–20689.
30 F. Hu, L. Shi and W. Min, *Nat. Methods*, 2019, **16**, 830–842.
31 S. F. El-Mashtoly, D. Petersen, H. K. Yosef, A. Mosig, A. Reinacher-Schick, C. Kötting and K. Gerwert, *Analyst*, 2014, **139**, 1155.
32 W. J. Tipping, M. Lee, A. Serrels, V. G. Brunton and A. N. Hulme, *Chem. Sci.*, 2017, **8**, 5606–5615.
33 J. Seidel, Y. Miao, W. Porterfield, W. Cai, X. Zhu, S.-J. Kim, F. Hu, S. Bhattarai-Kline, W. Min and W. Zhang, *Chem. Commun.*, 2019, **55**, 9379–9382.
34 F. Hu, Z. Chen, L. Zhang, Y. Shen, L. Wei and W. Min, *Angew. Chem., Int. Ed.*, 2015, **54**, 9821–9825.
35 R. Long, L. Zhang, L. Shi, Y. Shen, F. Hu, C. Zeng and W. Min, *Chem. Commun.*, 2018, **54**, 152–155.
36 H. J. Lee, W. Zhang, D. Zhang, Y. Yang, B. Liu, E. L. Barker, K. K. Buhman, L. V. Slipchenko, M. Dai and J.-X. Cheng, *Sci. Rep.*, 2015, **5**, 7930.
37 F. Hu, L. Wei, C. Zheng, Y. Shen and W. Min, *Analyst*, 2014, **139**, 2312–2317.
38 L. E. Jamieson, J. Greaves, J. A. McLellan, K. R. Munro, N. C. O. Tomkinson, L. H. Chamberlain, K. Faulds and D. Graham, *Spectrochim. Acta, Part A*, 2018, **197**, 30–36.
39 L. Wei, F. Hu, Y. Shen, Z. Chen, Y. Yu, C.-C. Lin, M. C. Wang and W. Min, *Nat. Methods*, 2014, **11**, 410–412.
40 H. Yamakoshi, A. F. Palonpon, K. Dodo, J. Ando, S. Kawata, K. Fujita and M. Sodeoka, *Chem. Commun.*, 2014, **50**, 1341–1343.
41 J. Reijenga, A. van Hoof, A. van Loon and B. Teunissen, *Anal. Chem. Insights*, 2013, **8**, ACI.S12304.
42 J. A. Thomas, R. N. Buchsbaum, A. Zimniak and E. Racker, *Biochemistry*, 1979, **18**, 2210–2218.
43 D. G. Nicholls and S. J. Ferguson, in *Bioenergetics*, Elsevier, 2013, pp. 13–25.
44 M. R. James-Kracke, *J. Cell. Physiol.*, 1992, **151**, 596–603.
45 L. E. Jamieson, C. Wetherill, K. Faulds and D. Graham, *Chem. Sci.*, 2018, **9**, 6935–6943.
46 D. Lagadic-Gossmann, L. Huc and V. Lecureur, *Cell Death Differ.*, 2004, **11**, 953–961.
47 M. A. Barry, J. E. Reynolds and A. Eastman, *Cancer Res.*, 1993, **53**, 2349–2357.
48 The choice of PC3 cells was based on previous experience using this cell line. See ref. 45.
49 M. J. Frisch, G. W. Trucks, H. B. Schlegel, G. E. Scuseria, M. A. Robb, J. R. Cheeseman, G. Scalmani, V. Barone, B. Mennucci and G. A. Petersson, Available: https://gaussian.com/g09citation.
50 C. Mongay and V. Cedra, *Ann. Chim.*, 1974, **64**, 409–412.
51 W. J. Gelsema, C. L. de Ligny, A. G. Remijnse and H. A. Blijleven, *Recl. Trav. Chim. Pays-Bas*, 2010, **85**, 647–660.
52 T. Myochin, K. Kiyose, K. Hanaoka, H. Kojima, T. Terai and T. Nagano, *J. Am. Chem. Soc.*, 2011, **133**, 3401–3409.